How to cite: *Angew. Chem. Int. Ed.* **2025**, *64*, e202509303
doi.org/10.1002/anie.202509303

Nitrate Reduction **Hot Paper**

Continuous Intermediates Spillover Boosts Electrochemical Nitrate Conversion to Ammonia over Dual Single-Atom Alloy

Wei Ye[+], Yuanhui Yao[+], Xiaofei Wei[+], Mengqiu Xu[+], Shuang Zhao, Wei Wang, Gan Jia, Fangna Dai, Peng Gao,* Xiaoqing Lu, Xiaogang Li, Baojuan Xi, Nana Wang, and Shenglin Xiong**

Abstract: Electrochemical nitrate conversion to ammonia driven by sustainable green electricity is regarded as a promising supplement to the traditional Haber–Bosch process. However, it is still restricted by the low NH_3 yield rate and Faradaic efficiency. Here, we propose a continuous intermediates spillover strategy by constructing dual single-atom alloy to boost ammonia yield rate and Faradaic efficiency. The intermediates continuously spill over back and forth on the atomically dispersed Mo and Fe sites in Pd lattice, which adaptively experiences low energy barrier for each elementary step in nitrate conversion. As a result, the synthesized dual single-atom alloy metallene delivered an NH_3 yield rate of 13.4 mol $g_{cat.}^{-1}$ h^{-1}, and Faradaic efficiency of 94.6%, as well as remarkable cycling stability of 300 h. Furthermore, the dual single-atom alloy metallene was assembled into a zinc-nitrate battery as the cathode, which delivered an output voltage of 1.477 V, and the maximum output power density of 13.4 mW cm^{-2}.

Introduction

Ammonia (NH_3) plays an extremely important role in modern society, which is the raw material for the manufacture of nitrogen fertilizer, nitrogen-containing medicines, polymer materials, dyes and so on.[1–3] The global annual ammonia production has reached 235 million tons in 2019.[4] Up to now, industrial ammonia synthesis heavily relies on the century-old Haber–Bosch process, in which nitrogen (N_2) and hydrogen (H_2) are reacted to NH_3 using Fe-base material as a catalyst at harsh conditions (temperature 400 °C–500 °C, pressure 150–300 atm). Due to the harsh conditions and the huge ammonia production in the world, NH_3 synthesis industry consumes about 1%–2% of the global annual energy demand, accounting for about 1% of the carbon dioxide (CO_2) emission.[5,6] Hence, it is very urgent to develop a green, sustainable and energy-saving ammonia synthesis technology to partially replace the Haber–Bosch process.

Electricity driven nitrates reduction reaction (NO_3RR) is regarded as a powerful complement to the traditional Haber-Bosch process toward large-scale ammonia synthesis. Benefitting from the extremely high solubility of the nitrate ions, and relative low bond energy of N=O (204 kJ mol^{-1}), the ammonia generation kinetics of NO_3RR is increased by 3–4 orders of magnitude with relatively low energy input in comparison to the fascinating nitrogen reduction reaction (NRR).[7–16] Moreover, nitrates are widely existed in nature, mainly derived from industrial wastewater, domestic sewage, livestock manure and nuclear industry wastewater.[17] Beyond that, NO_3RR possesses high equilibrium potential of 0.69 V versus the reversible hydrogen electrode (RHE), higher than that of the oxygen reduction reaction (ORR, 0.4 V) in Zn–air/oxygen batteries.[18,19] As such, integrating of NO_3RR as a cathode coupled with zinc oxidation as an anode to assemble zinc-nitrate battery, can achieve the goal of one stone and three birds, namely the removal of nitrates, obtaining valuable ammonia and outputting electrical energy.[20–23] However, the current electrochemical NO_3^--to-NH_3 conversion is still restricted by the low NH_3 yield rate and Faradaic efficiency (FE).

Typically, NO_3^--to-NH_3 conversion is a process involving nine protons and eight electrons (NO_3^- + $9H^+$

[*] Dr. W. Ye[+], Y. Yao[+], S. Zhao, Dr. W. Wang, Dr. G. Jia, Prof. P. Gao
Key Laboratory of Organosilicon Chemistry and Material Technology, Ministry of Education, Zhejiang Key Laboratory of Organosilicon Material Technology, College of Material, Chemistry and Chemical Engineering, Hangzhou Normal University, Hangzhou, Zhejiang 311121, China
E-mail: gaopeng@hznu.edu.cn

Dr. X. Wei[+], Prof. F. Dai, Prof. X. Lu
School of Materials Science and Engineering, China University of Petroleum (East China), Qingdao 266580, China
E-mail: fndai@upc.edu.cn

Dr. X. Li, Prof. B. Xi, Prof. S. Xiong
School of Chemistry and Chemical Engineering, Shandong University, Jinan 250100, China
E-mail: chexsl@sdu.edu.cn

Dr. M. Xu[+]
Laboratory of Advanced Materials, Department of Chemistry and Shanghai Key Laboratory of Molecular Catalysis and Innovative Materials, Fudan University, Shanghai 200438, China

Dr. N. Wang
Centre for Clean Energy Technology, School of Mathematical and Physical Sciences, Faculty of Science, University of Technology Sydney, Sydney, NSW 2007, Australia

[+] These authors contributed equally to this work.

Additional supporting information can be found online in the Supporting Information section

$+ 8e^- \rightarrow NH_3 + 3H_2O$), in which the various N-intermediates undergo step-by-step hydrogenation and dehydration on the catalyst surface, ultimately convert to NH_3. Currently, various strategies, including alloying,[12,20] heteroatom doping,[18] heterojunction,[11,22] defect engineering[23] have been put forward, aiming to reduce the energy barrier of the rate-determining step (RDS) of NO_3RR.[24] Nevertheless, the influence of the energy barriers of the non-RDSs in NO_3RR on the overall performance was ignored. Inspired by the water flow process in nature, which always spontaneously experiences the lowest energy path, the overall NO_3RR performance is bound to be optimal if each elementary step also undergoes the lowest energy barrier. For the multi-intermediates and multi-steps involved reduction process, multiple active centers nor single active center are essential to achieve the lowest energy barrier required for each conversion step as much as possible.[25]

Here, we put forward a novel continuous intermediates spillover strategy to enhance proton-coupled electron transfer process by constructing dual single-atom molybdenum (Mo_1) and iron (Fe_1) alloy metallene. Previous reports have confirmed that Mo and Fe single-atom sites could achieve the tandem NO_3RR, which achieved high NH_3 FE.[26,27] In addition, the Pd metallene was chosen as the carrier due to the high specific surface area, tunable electronic structure, which endowed high electrochemical performance in catalysis.[28] The atomically dispersed Mo and Fe atoms in Pd matrix facilitated N-intermediates hop back and forth between Mo and Fe sites in searching of the lower energy barrier for each elementary step, which was confirmed by in situ spectroscopic characterizations and theoretical calculations. Beyond that, atomic Mo and Fe doping regulated the interfacial water network structure to inhibit the too fast water splitting kinetics, which synchronously guaranteed high NH_3 yield rate and FE. As a result, the synthesized dual single-atom alloy metallene displayed greatly enhanced NH_3 yield rate and NH_3 FE compared with that of the counterpart metallenes.

Results and Discussion

As demonstrated in Figure 1a, atomically dispersed Mo and Fe atoms in Pd metallene matrix were synthesized using an one-pot wet-chemical approach, in which $Pd(acac)_2$, $Fe_2(CO)_9$, and $Mo(CO)_6$ were co-reduced at 80 °C for 12 h. Carbon monoxide (CO) molecules in situ released from $Fe_2(CO)_9$ and $Mo(CO)_6$ adsorbed tightly on Pd-rich alloy surface, which resulted in the formation of ultrathin Pd-rich nanosheet, i.e., Pd-rich trimetallene, denotes as Mo_1Fe_1Pd trimetallene.[28] As a control, atomically dispersed iron (Fe_1Pd) or molybdenum (Mo_1Pd) atoms bimetallenes, and Pd metallene were synthesized with a similar synthetic process (Figures S1 and S2). Powder X-ray diffraction (XRD) patterns show that both Mo_1Fe_1Pd and the control samples possess face-centered cubic (*fcc*) structure, consistent with that of *fcc* Pd (JCPDS no. 46–1043, Figure 1b). As determined by inductively coupled plasma-mass spectrometry (ICP-MS), the molar ratios of Pd, Fe, and Mo were 90:8:2. Transmission electron microscopy (TEM) and high-angle annular dark-field scanning TEM (HAADF-STEM) images reveal that the sample is dominated by ultrathin nanosheet structure (Figures 1c and S1a) with average lateral size of about 100–200 nm. The thickness of the trimetallene is only 1.8 nm, determined by atomic force microscopy (AFM) measurement (Figure 1d), coincided with the result determined by TEM characterization (the insert in Figure 1c), further confirming the metallene structure. Atomic-resolution aberration-corrected HAADF-STEM image (Figure 1e) displays clear two-dimensional atom arrangement with a lattice distance of 0.195 nm at the edge of the metallene, assigning to the (100) plane of Mo_1Fe_1Pd. EDS elemental mapping images in Figure 1f demonstrate the uniform distribution of Mo, Fe, and Pd across the entire metallene, further verifying the trimetallic alloy structure. X-ray photoelectron spectroscopy (XPS) result of Mo_1Fe_1Pd trimetallene indicates that Mo 3d spectrum (Figure 1g) displays two pairs of peaks with binding energy located at 227.2, 229.7 eV and 232.5, 235.8 eV, assigning to $3d_{5/2}$ and $3d_{3/2}$ of Mo^0 and Mo^{6+}, respectively.[29,30] Fe 2p spectrum (Figure 1h) between 710 and 735 eV suggests the surface Fe element mainly appeared in the form of oxidized species, possibly due to the surface oxidation of Mo_1Fe_1Pd.[31] Notably, Pd was mainly existed in the form of metallic state (Figure S3).

To decode the exact fine structure of molybdenum and iron elements in the sample, Mo_1Fe_1Pd trimetallene sample was further characterized by synchrotron radiation-based X-ray absorption fine structure (XAFS) spectroscopy. Figure 2a shows Mo K-edge X-ray absorption near edge structure (XANES) spectroscopy in reference with Mo foil and MoO_2. Mo extended XAFS (EXAFS) spectra were obtained by Fourier transform of Mo K-edge, in which Mo—Mo bond was absent in Mo_1Fe_1Pd sample (Figure 2b and Table S1). Mo—Pd (2.72 Å) and Mo—Fe (2.50 Å) bonds were resolved in the first shell with a coordination number (CN) of 3.7 and 1.7, respectively. The fine structure was further confirmed by fitting the k^3-weighted Fourier transformed EXAFS spectra and k space results (Figures S4a and S5a). The results indicate that Mo atoms are atomically dispersed in PdFe alloy matrix. Figure 2c,d shows the Fe K-edge XANES and EXAFS spectra of Mo_1Fe_1Pd trimetallene sample in comparison to Fe foil and FeO, respectively. Similar to Mo case, Fe—Fe bonds were absent, and Pd—Fe (bond length 2.80 Å, CN 1.6) and Fe—O bonds (bond length 1.96 Å, CN 3.1) were resolved. The results suggest that Fe is also atomically dispersed in PdMo alloy lattice. Notably, the existence of Fe—O bonds suggests Fe element was partially oxidized in the air, consistent with that of XPS results. The Fe fine structure was also verified by fitting the k^3-weighted Fourier transformed EXAFS spectra and k space results (Figures S4b and S5b). Pd K-edge XANES and EXAFS spectra (Figures 2e,f, S4c, and S5c) resolve Pd—Pd and Pd—Mo/Fe bonds. Then, wavelet transforms (WT) analysis of the Mo, Fe, and Pd K-edge EXAFS oscillations of Mo_1Fe_1Pd trimetallene sample was performed in reference with MoO_2, Mo foil, Fe foil, FeO, and Pd foil (Figure 2g). Two-dimensional contour maps of Mo_1Fe_1Pd sample resolve Mo—Pd, Mo—Fe, Pd—Pd bonds, while Mo—Mo and Fe—Fe bonds are absent. Putting together the above results, we conclude that Mo and Fe atoms are atomically dispersed in Pd-rich alloy lattice, namely dual single-atom Mo and Fe alloy.

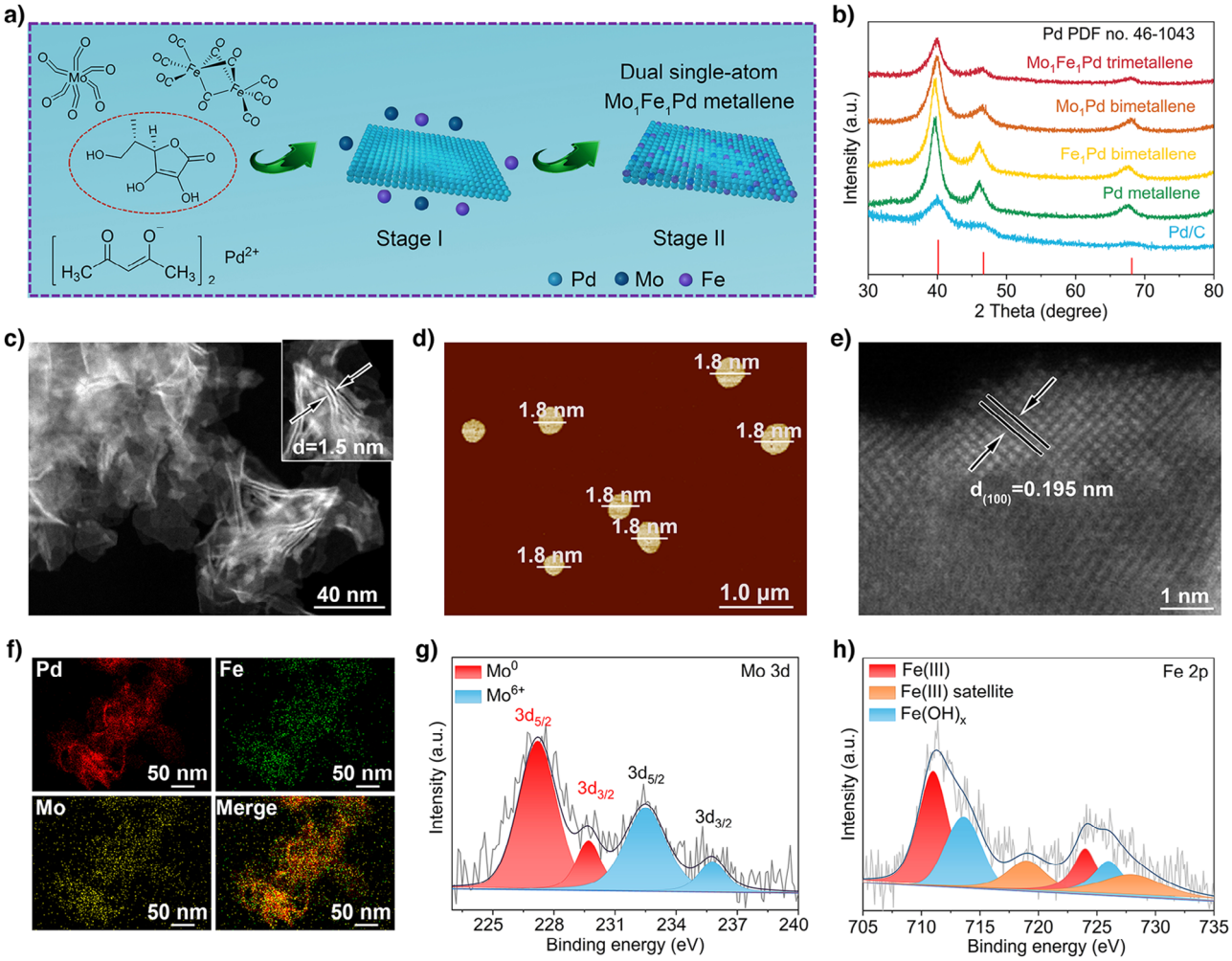

Figure 1. a) Schematic illustration of the synthesis of Mo_1Fe_1Pd trimetallene. b) XRD patterns. c) HAADF-STEM image, d) AFM image, e) atomic-resolution HAADF-STEM image, f) EDS elemental mapping profiles of Mo_1Fe_1Pd trimetallene, Pd (red), Fe (green) and Mo (yellow) distribution. High-resolution g) Mo 3d and h) Fe 2p spectra. The insert in c) is the enlarged HAADF-STEM image of Mo_1Fe_1Pd trimetallene.

Electrochemical NO_3RR performance of Mo_1Fe_1Pd trimetallene was evaluated in an H-type cell using a typical three-electrode system at room temperature. Linear sweep voltammetry (LSV) tests were first performed in the mixture solution of KOH and KNO_3 to assess the current response. As shown in Figure 3a, the onset potential for Mo_1Fe_1Pd trimetallene is positively shifted from 0.32 (Pd metallene), 0.43 (Fe_1Pd bimetallene), 0.48 (Mo_1Pd bimetallene) to 0.55 V versus RHE, suggesting that Mo_1Fe_1Pd is more active in NO_3RR. As expected, the current density in NO_3RR of Mo_1Fe_1Pd trimetallene is obvious higher than that of Mo_1Pd, Fe_1Pd bimetallenes, and Pd metallene. The results indicate that alloying dual single-atom Mo and Fe in Pd lattice indeed strengthens NO_3RR performance of Pd metallene. Notably, the synergistic effect of dual single-atom Mo and Fe atoms doping for NO_3RR was confirmed by altering Mo and Fe contents in Mo_1Fe_1Pd trimetallene (Figures S6 and S7), and discussed in detail in the following section. Upon confirming the optimal Mo and Fe content, potential-dependent ammonia yield rates (Figures 3b and S8) and ammonia FEs (Figure 3c) were obtained after electrolysis at the fixed potentials. Obviously, NH_3 yield rates and NH_3 FEs all gradually increased as the applied potentials negatively shifted from −0.1 to −0.7 V versus RHE for all the samples. Mo_1Fe_1Pd trimetallene delivered much higher NH_3 yield rates than that of Fe_1Pd, Mo_1Pd bimetallenes, and Pd metallene samples over the entire potential range. The maximum NH_3 yield rate of Mo_1Fe_1Pd trimetallene reached 13.4 mol $g_{cat.}^{-1}$ h^{-1} at −0.7 V, which was about 4.8- and 1.5-fold higher than that of Pd metallene (2.8 mol $g_{cat.}^{-1}$ h^{-1}) and Fe_1Pd bimetallene (9.1 mol $g_{cat.}^{-1}$ h^{-1}), respectively. Consistent with the activity, NH_3 FEs of Mo_1Fe_1Pd trimetallene all surpassed Fe_1Pd, Mo_1Pd bimetallenes, and Pd metallene in the potential range of −0.1 to −0.7 V. Impressively, Mo_1Fe_1Pd trimetallene delivered a high NH_3 FE of 94.6% at −0.7 V, much higher than that of Fe_1Pd (84.9%), Mo_1Pd (71.5%) bimetallenes, and Pd metallene (47.8%). The approaching 100% NH_3 FE of Mo_1Fe_1Pd trimetallene suggests that the competing hydrogen evolution reaction (HER) and the by-products in NO_3RR are almost inhibited (Figures S9–S11), which is vital important in real-world applications. To confirm the accuracy of the above NH_3 quantitative results, the yielded NH_3 in the electrolyte

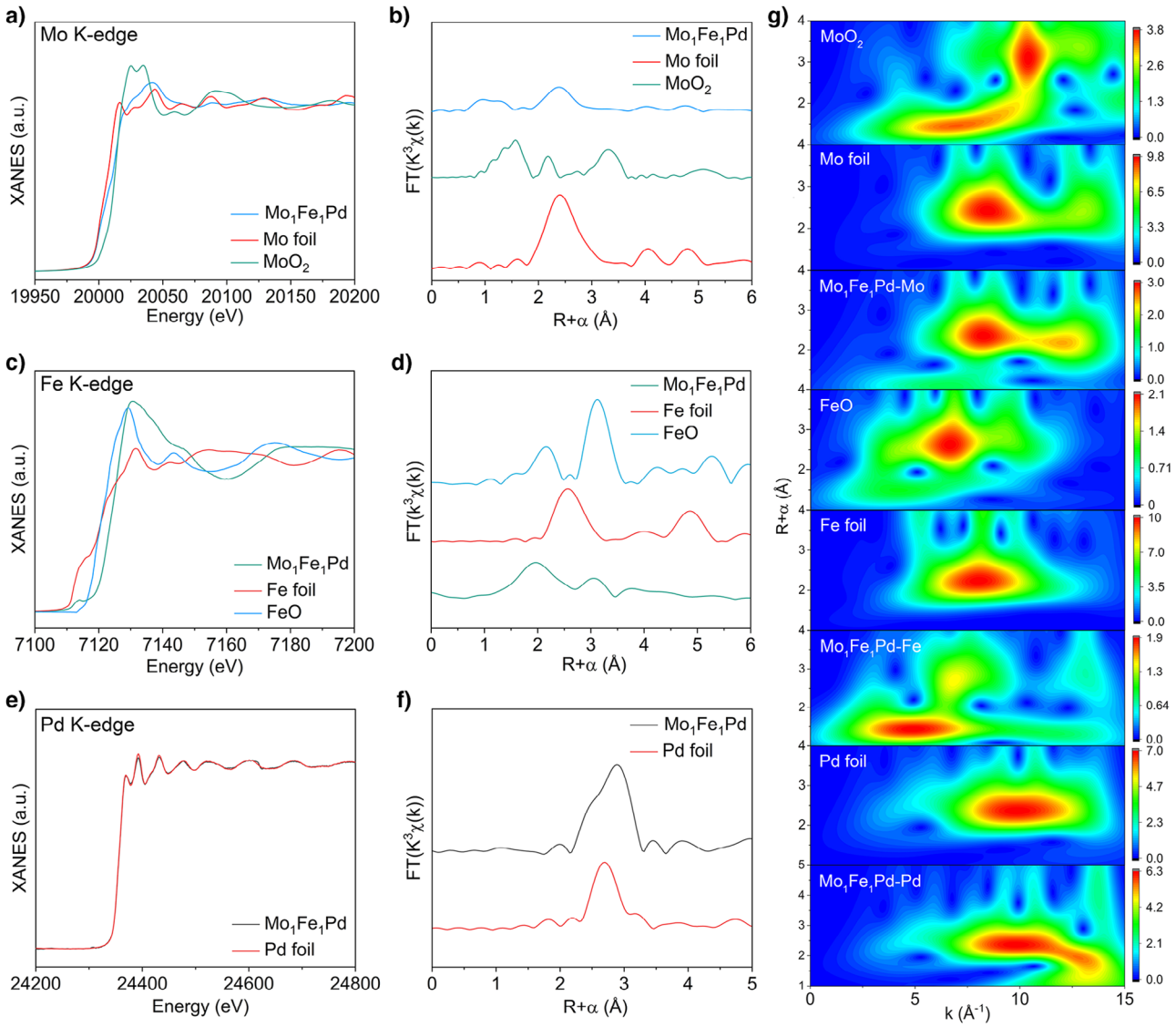

Figure 2. Normalized a) Mo K-edge, c) Fe K-edge and e) Pd K-edge XANES spectra of Mo_1Fe_1Pd trimetallene in comparison to Mo foil, MoO_2, Fe foil, FeO and Pd foil respectively. k^3-weighted Fourier-transform b) Mo K-edge, d) Fe K-edge and f) Pd K-edge EXAFS spectra. g) Wavelet transforms of the k^2-weighted Mo in reference with Mo foil and MoO_2, k^2-weighted Fe in reference with Fe foil and FeO, and k^2-weighted Pd in reference with Pd foil.

was further spectrographically quantified with indophenol blue assay, and the results are consistent (Figure S12).

In industrial scenarios, durability is an important parameter for catalyst assessment. In H-type cell, Mo_1Fe_1Pd trimetallene could sustain continuous thirty cycles at −0.7 V, NH_3 yield rates and NH_3 FEs were stable without obvious activity decay (Figure S13). To further assess the stability, the catalyst was further characterized by XRD pattern and TEM measurement after durability test. The crystal structure and the morphology of the Mo_1Fe_1Pd trimetallene were well maintained (Figure S14). EDS mapping images confirmed the uniform distribution of the elements, and XPS results revealed the valence states of the elements were well sustained, confirming the rigidity of the catalyst (Figures S15 and S16). In view of the excellent NO_3RR performance of Mo_1Fe_1Pd trimetallene, the catalyst was further evaluated in a flow cell with the volume of the electrolyte (1 M KNO_3 + 1 M KOH) amplified 12.5 times (500 mL, Figure S17), simulating the industrial NO_3RR scenarios. Amazingly, Mo_1Fe_1Pd trimetallene electrode could be stably operated at a total current density (j_{total}) of about 225 mA for 300 h (Figure 3d). In which, the yielded NH_3 in the electrolyte showed a linear relationship with the electrolysis time. Finally, 0.32 mol NH_3 was obtained after 300 h electrolysis with nitrate ions conversion of 64.0%. More importantly, NH_3 FEs were maintained above 80% during the entire device operation process. After the long-term of electrolysis, NH_3 in the electrolyte was stripped out by bubbling Ar flow and collected downstream with a diluted HCl solution (Figure S18).[32] Finally, 9.36 g of high-purity of NH_4Cl powder was obtained by evaporating the hydrochloric acid solution, the NH_4Cl powder was confirmed by XRD pattern (Figure 3e). Mo_1Fe_1Pd trimetallene catalyst exceeds the current state-of-the-art Mo and Fe- based electrocatalysts as

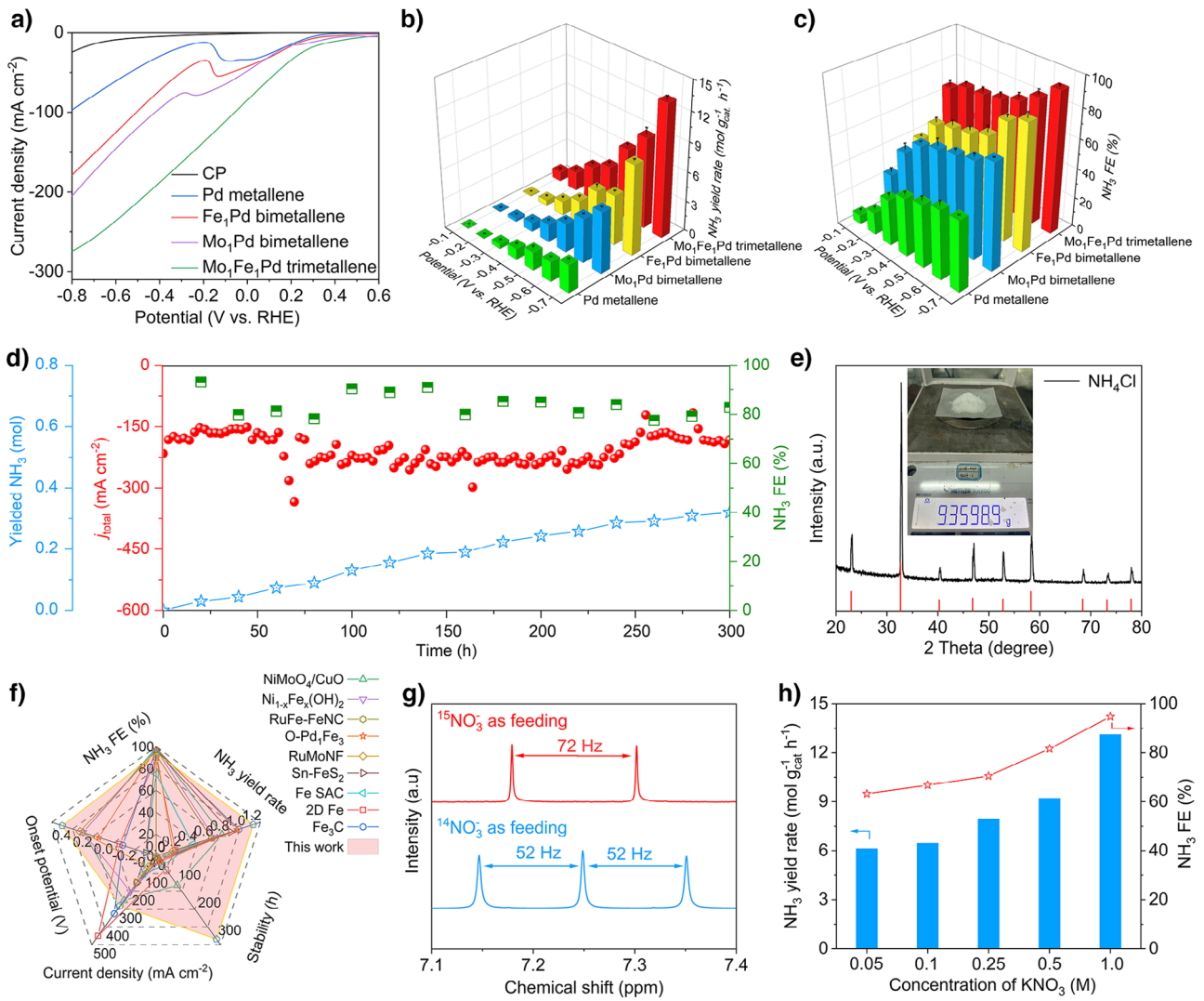

Figure 3. a) LSV curves in NO_3RR. b) Potential-dependent NH_3 yield rates and c) the corresponding NH_3 FEs of Mo_1Fe_1Pd trimetallene in reference with Fe_1Pd, Mo_1Pd bimetallenes, and Pd metallene. d) Long-term cycling stability test, and the time-resolved NH_3 yielded amount and NH_3 FEs of Mo_1Fe_1Pd trimetallene in a flow cell. e) XRD pattern of the obtained NH_4Cl powder after long-term cycling test, the inset is the photograph of the obtained NH_4Cl powder. f) The comparison of electrochemical NO_3RR performance of Mo_1Fe_1Pd trimetallene with the recently reported electrocatalysts. g) ^{1}H-NMR spectra of the electrolytes using $K^{15}NO_3$ or $K^{14}NO_3$ as N-resource in NO_3RR test. h) NH_3 yield rates and NH_3 FEs of Mo_1Fe_1Pd trimetallene at different concentrations of KNO_3 and −0.7 V. b), c) Error bars in accordance with the standard deviation of at least three independent measurements.

summarized in Figure 3f in terms of the onset potential, NH_3 yield rate, NH_3 FE, current density and service life (Table S2).

Then, ^{15}N isotope labeling experiment was carried out to confirm that the produced NH_3 was really rooted from NO_3RR, not contamination from nitrogenous precursors (Figure 3g). Nuclear magnetic resonance spectrum (^{1}H-NMR) of the electrolyte shows a double peak between 7.1–7.4 ppm with a coupling constant of 72 Hz using $K^{15}NO_3$ as N-resource, the characteristic signal of $^{15}NH_4^+$.[33] As a control, a triplet peak with a coupling constant of 52 Hz arise in ^{1}H-NMR spectrum with $K^{14}NO_3$ as N-feeding. The above result irrefutably confirms the yielded NH_3 indeed come from NO_3RR. Moreover, Mo_1Fe_1Pd trimetallene delivers excellent NO_3RR performance in a wide range of NO_3^- concentrations (Figure 3h) and pH (Figure S19).

In the field, the direct conversion of nitrates in wastewater into ammonia to provide nitrogen source for crops is the most direct way for nitrogen cycle. Using solar power to drive the above device can not only reduce the cost of electricity, but also realize the self-driven sustainable operation of ammonia synthesis. This requires the stable operation of the electrolyzer over a wide voltage range. Under this scenario, we further simulated the ammonia production by electrolysis of nitrates driven by solar energy (Figure S20). A commercial silicon solar panel (1.9 W) illuminated by xenon lamp (100 mW cm^{-2}) was employed to power ammonia electrosynthesis using Mo_1Fe_1Pd trimetallene as a catalyst in the wild environment. As expected, the yielded NH_3 amounts showed a linear relationship with the illumination time, and an average NH_3 yield rate reached

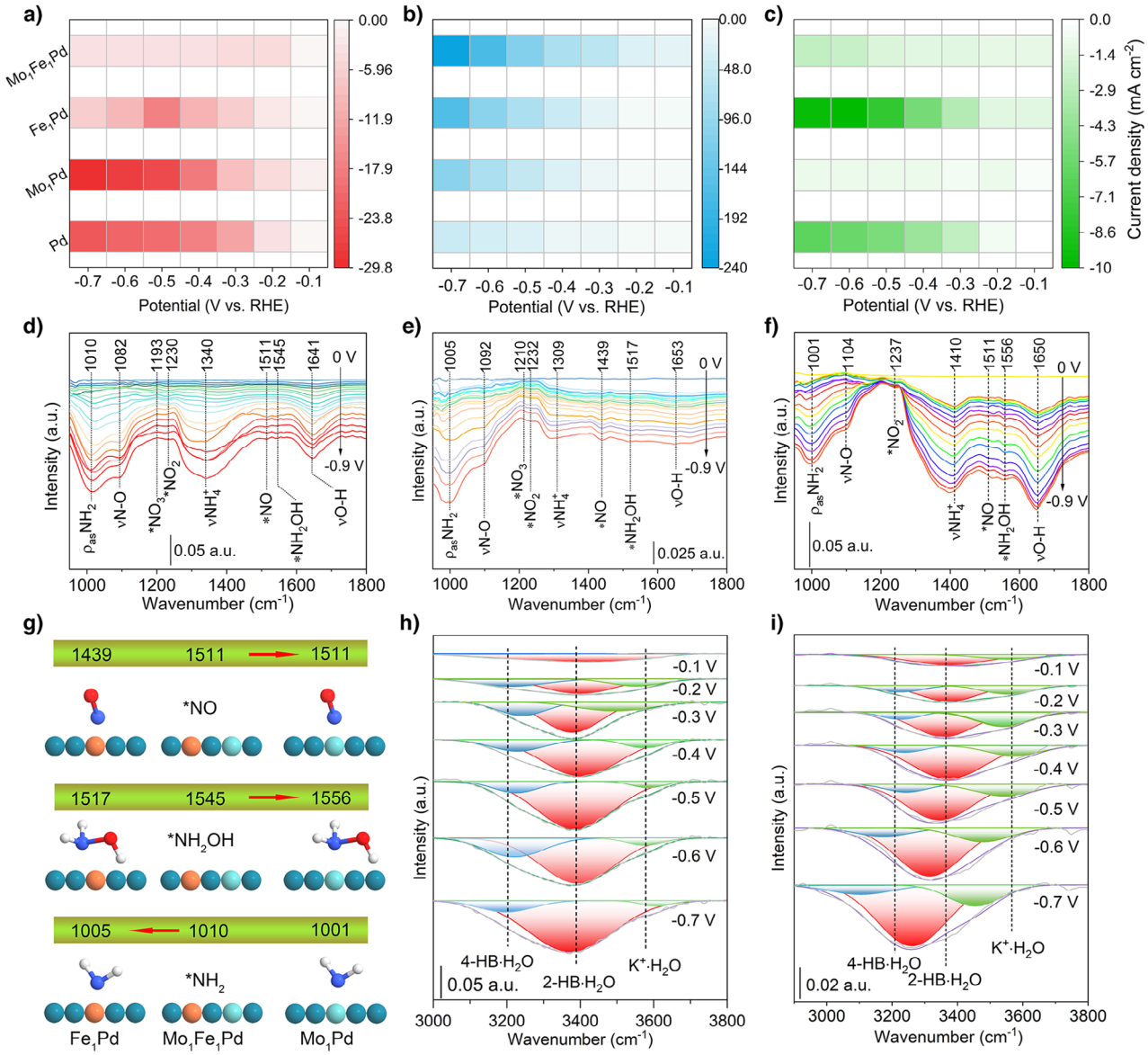

Figure 4. Potential-dependent partial current densities of a) $j_{NO_2^-}$, b) j_{NH_3} and c) j_{H_2} for Mo_1Fe_1Pd trimetallene in reference with Mo_1Pd, Fe_1Pd bimetallenes, and Pd metallene. Potential-resloved ATR-FTIR spectra, d) Mo_1Fe_1Pd trimetallene, e) Fe_1Pd, f) Mo_1Pd bimetallenes. g) Schematic illustration of the intermediates hopping on the catalyst surface confirmed by in situ ATR-FTIR spectra. Potential-dependent interfacial water structure signal of h) Mo_1Fe_1Pd and (i) Fe_1Pd metallene determined by ATR-FTIR.

2.96 mol $g_{cat.}^{-1}$ h^{-1}, demonstrating the potential application prospects.

Upon assessing the NO_3RR performance, it is essential to decode the specific role of Mo and Fe dual single-atom alloy in ammonia electrosynthesis. Generally, NO_3RR usually follows a two-step tandem reduction process, i.e., $NO_3^- + 2H^+ + 2e^- \rightarrow NO_2^- + H_2O$ (process i) and then $NO_2^- + 7H^+ + 6e^- \rightarrow NH_3 + 2H_2O$ (process ii).[34] To explore the role of atomic Mo and Fe sites in Pd lattice on NO_3RR performance, partial current density (j) is the most intuitive evidence. Figure 4a–c shows the potential-dependent partial current densities of NO_2^- ($j_{NO_2^-}$), ammonia (j_{NH_3}) and HER (j_{H_2}) for Mo_1Fe_1Pd trimetallene in comparison to Fe_1Pd, Mo_1Pd bimetallenes, and Pd metallene, respectively (Figure S21). For $NO_3^- \rightarrow NO_2^-$ conversion, the $j_{NO_2^-}$ arranges as follow: $Mo_1Pd > Pd > Fe_1Pd > Mo_1Fe_1Pd$ (Figure 4a). In contrast, the j_{NH_3} is listed as $Mo_1Fe_1Pd > Fe_1Pd > Mo_1Pd > Pd$. By comparing the results of Fe_1Pd, Mo_1Pd, and Pd samples, it is concluded that alloying single-atom Mo in Pd matrix greatly enhances $j_{NO_2^-}$, while single-atom Fe in Pd lattice increases j_{NH_3} and weakens $j_{NO_2^-}$. Considering the promotion effect of single-atom Mo and Fe on process i and ii, alloying dual single-atom Mo and Fe in Pd lattice may cascade $NO_3^- \rightarrow NO_2^-$ (by Mo) and $NO_2^- \rightarrow NH_3$ (by Fe) processes in NO_3RR. The above supposition was verified by the smallest $j_{NO_2^-}$ and the largest j_{NH_3} of Mo_1Fe_1Pd trimetallene.

As a major side reaction, water splitting process not only releases hydrogen, but also provides active hydrogen (*H) atoms. As nine *H are involved in NO_3RR, therefore the

kinetics of water splitting greatly determines the final NH_3 yield rate and NH_3 FE, especially in the more negative potential area. On the one hand, the sluggish kinetics of water splitting process is not enough to provide sufficient *H for the subsequent deoxyreduction processes, resulting in weakened NH_3 yield rate. However, the too fast kinetics of water splitting boosts *H formation and aggravates HER, leading to an awful NH_3 FE. The trade-off water splitting activity directly determines NH_3 yield rate and NH_3 FE. As shown in Figure 4c, j_{H_2} is declined for Mo_1Fe_1Pd trimetallene in comparison to Fe_1Pd bimetallene and Pd metallene, comparable with that of Mo_1Pd bimetallene. The possible reason may be due to the regulated M—H (M=Pd, Mo, and Fe) bond strength after alloying single-atom Mo in Pd-rich metallene, and/or the optimized interfacial water network structure.[35,36] Putting together the above results, alloying dual single-atom Mo and Fe in Pd not only cascades $NO_3^- \rightarrow NO_2^-$ and $NO_2^- \rightarrow NH_3$ conversions, but also modulates the hydrogen bond to restrain the major competing HER. As a result, the N-selectivity of NH_3 was greatly enhanced, and NO_2^- was completely suppressed for Mo_1Fe_1Pd trimetallene (Figure S22).

Beyond that, the chemical redox reaction of Pd and NO_3^- also contributed the NO_2^- formation in NO_3RR, similar with the role of single-atom Mo. The oxidized Pd species was further reduced to metallic Pd in the operation of NO_3RR (Figures S23–S25).[37] Based on the above analysis, the detailed mechanism of dual single-atom Mo and Fe in Pd for NO_3RR was summarized in Figure S26. Moreover, electrochemical active surface area (ECSA) was also obtained, Mo_1Fe_1Pd trimetallene delivered a higher ECSA than that of Mo_1Pd, Fe_1Pd bimetallenes, and Pd metallene, which also contributed to the enhanced NO_3RR performance (Figure S27).

To further investigate why the single-atom Mo and Fe sites can cascade NO_3RR, in situ spectroscopic characterizations were carried out to clarify the reaction pathway. Potential-dependent in situ attenuated total reflection flourier transform infrared spectroscopy (ATR-FTIR) measurements were conducted both for Mo_1Fe_1Pd, Mo_1Pd, Fe_1Pd samples. Figure 4d–f shows the potential-resolved ATR-FTIR spectra in NO_3RR from 0 to −0.9 V (V versus RHE) of Mo_1Fe_1Pd, Fe_1Pd and Mo_1Pd samples, respectively. As shown in Figure 4d, the signal of $*NO_3$ and $*NO_2$ located at 1193 and 1230 cm^{-1} was emerged at −0.1 V, indicating the conversion of $*NO_3$ to $*NO_2$.[38,39] Then, three obvious vibration peaks located at 1010, 1082 and 1340 cm^{-1} arose at −0.2 V, which were attributed to $\rho_{as}NH_2$, νN—O and νNH_4^+, respectively, suggesting the formation of NH_3.[39–41] Compared with $*NO_2$, the intensity of $\rho_{as}NH_2$ and νNH_4^+ increased sharply when the applied potential was lower than −0.35 V, suggesting the accelerated conversion of NO_3^--to-NH_3. The result well explains the enhanced j_{NH_3} and NH_3 FE. Two tiny peaks located at 1511 and 1545 cm^{-1} appeared at −0.65 V, assigning to *NO and $*NH_2OH$, respectively.[42,43] The result indicates that NO_3RR may undergo $*NO_2$-to-*NO pathway, and then to $*NH_2OH$, finally convert to NH_3. The peak located at 1641 cm^{-1} was assigned to νO-H of interfacial H_2O molecule.[44] The above possible pathway coincided with that of in situ Raman spectra in NO_3RR (Figure S28). Notably, the signal of the key intermediates was all emerged on Fe_1Pd bimetallene (Figure 4e), Mo_1Pd bimetallene (Figure 4f) and Pd metallene (Figure S29), suggesting the similar reaction pathway on Fe_1Pd, Mo_1Pd bimetallenes, and Pd metallene. That is to say dual single-atom Mo and Fe doping in Pd matrix does not change the reaction pathway of NO_3RR. Moreover, it should be emphasized that Mo_1Fe_1Pd sample delivered higher ATR-FTIR intensity than that of Fe_1Pd, Mo_1Pd bimetallenes, and Pd metallene, proofing the enhanced NO_3RR performance of Mo_1Fe_1Pd. As a stark contrast, only the signal of $\rho_{as}NH_2$ and νNH_4^+ with much lower intensity was observed on Pd metallene, further confirming the greatly enhanced NO_3RR performance of dual single-atom Mo and Fe alloy trimetallene.

In addition to the type and strength of the N-intermediates signal, it was observed the difference of the position for *NO, $*NH_2OH$ and $*NH_2$. Specifically, the signal of *NO arose at 1439 and 1511 cm^{-1} for Fe_1Pd and Mo_1Pd, respectively. While, the signal of *NO was located at 1511 cm^{-1} for Mo_1Fe_1Pd, coincided with that of Mo_1Pd (Figure 4g). As determined by XAFS results, Mo_1Fe_1Pd sample possesses two distinct sites, i.e., Mo and Fe sites, therefore, it is inferred that *NO could be adsorbed on Mo site for Mo_1Fe_1Pd sample. Accordingly, the ATR-FTIR signal of $*NH_2OH$ and $*NH_2$ were located at 1545 and 1010 cm^{-1} for Mo_1Fe_1Pd sample, more closer to that of Mo_1Pd and Fe_1Pd samples, respectively. The results indicate that $*NH_2OH$ could be adsorbed on Mo site, while $*NH_2$ was adsorbed on Fe site. Based on the above results, we infer that the N-intermediates occurs continuous spillover between Mo and Fe sites as the hydrogenation process proceeds. Obviously, the intermediates spillover was driven by energy, so that the intermediates conversions always experienced the lower energy barrier, as such electrochemical NO_3RR performance was boosted.

To further investigate the role of dual single-atom Mo and Fe alloy on the water splitting, the signal of the interfacial water structure between 3000 and 3800 cm^{-1} were truncated from the in situ ATR-FTIR spectra.[45] Figure 4h,i shows the potential-resolved interfacial water structure signal of Mo_1Fe_1Pd trimetallene and Fe_1Pd bimetallene, respectively, which were divided into three peaks by Gaussian fitting, i.e., 4-HB·H_2O (3200 cm^{-1}), 2-HB·H_2O (3400 cm^{-1}) and K^+·H_2O (3600 cm^{-1}).[46] Alloying single-atom Fe in Pd lattice facilitated the formation of K^+·H_2O due to the oxytropism of Fe element (Figures S30 and S31), consistent with previous results.[47] As such, Fe_1Pd bimetallene delivered higher ratio of K^+·H_2O signal than that of Pd metallene. Generally, K^+·H_2O improves the kinetics of water splitting reaction due to the lower activation energy, and thus more active hydrogen atoms are formed on the catalyst surface.[48] The results well explain the enhanced NO_3RR performance and the enlarged j_{H_2} for Fe_1Pd sample. Further alloy single-atom Mo in Fe_1Pd alloy decreased the proportion of the K^+·H_2O for Mo_1Fe_1Pd trimetallene. As a result, the fast kinetics of water cracking to produce *H was decreased, accordingly, the coupling of *H and *H to release hydrogen was inhibited. Finally, enhanced NH_3 yield rate and the approaching 100% NH_3 FE were synchronously achieved for Mo_1Fe_1Pd sample.

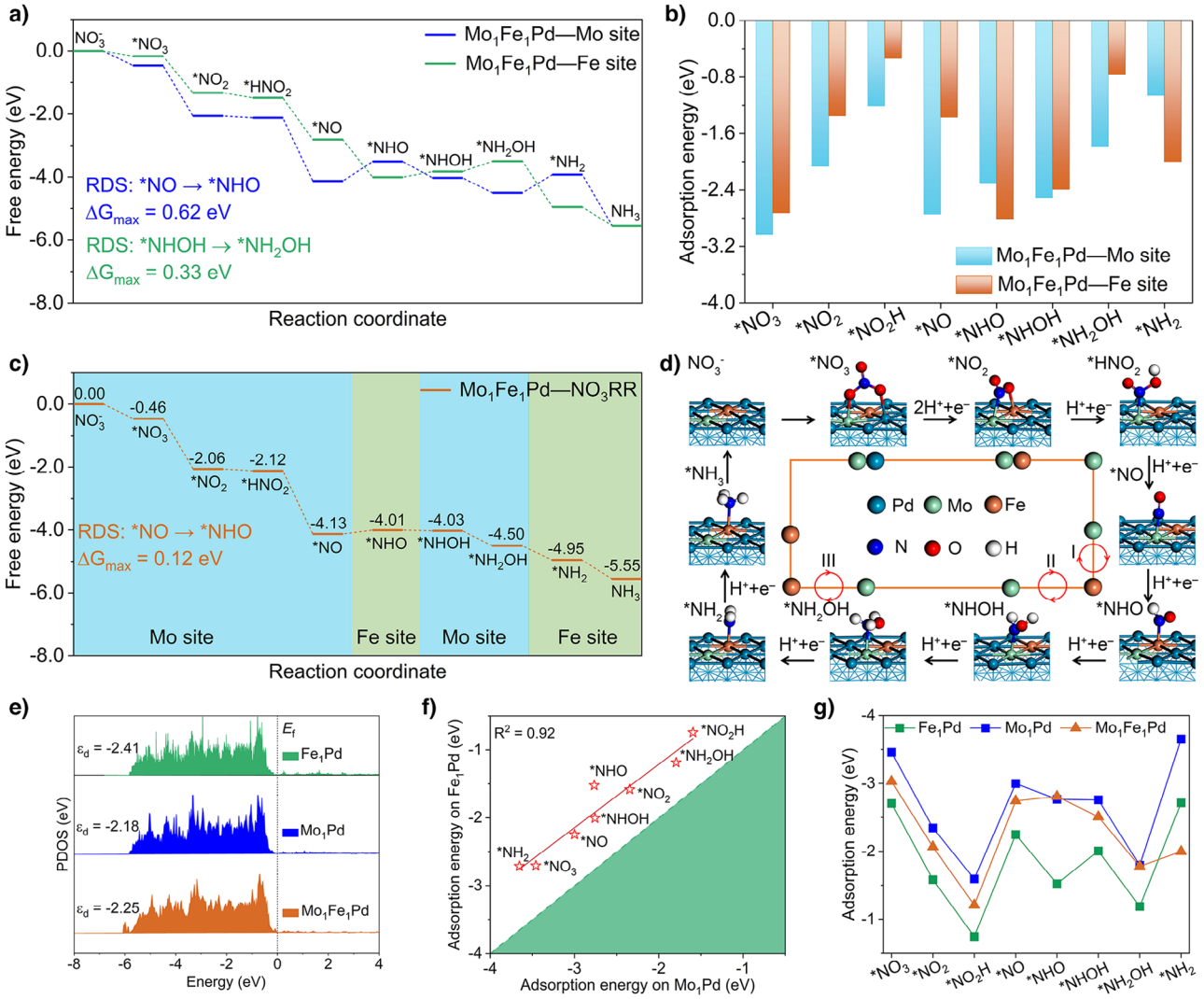

Figure 5. a) The Gibbs free energy diagrams for NO_3RR on different sites of Mo_1Fe_1Pd. b) Comparison of adsorption energies of reaction intermediates on different sites of Mo_1Fe_1Pd. c) The Gibbs free energy diagram for NO_3RR on Mo_1Fe_1Pd along the optimal pathway. d) The structural models of reaction intermediates of NO_3RR on Mo_1Fe_1Pd, and the demonstration of dynamic intermediates spillover between Mo and Fe sites. e) Projected density of states (PDOS) of Fe_1Pd, Mo_1Pd, Mo_1Fe_1Pd, and the corresponding d-band center values (ε_d, eV). f) Scaling relationship of adsorption energy of reaction intermediates between Fe_1Pd and Mo_1Pd. g) The adsorption energies of different reaction intermediates on Fe_1Pd, Mo_1Pd, and Mo_1Fe_1Pd surface.

Density functional theory (DFT) calculations were performed to further investigate the intrinsic mechanism of dual single-atom Mo and Fe doping in Pd metallene (Mo_1Fe_1Pd) for NO_3RR. According to the previous results, Pd metallene enclosed with (111) plane was employed as the slab.[28] The optimized structural models of Fe_1Pd, Mo_1Pd, and Mo_1Fe_1Pd metallenes showed that dissimilar metal atoms could be doped in Pd effectively and stably (Figure S32). Bader charge analysis indicated electron transfer was occurred from Mo and Fe atoms to the adjacent Pd atoms for Mo_1Fe_1Pd, and the electronic structure was effectively regulated. Considering the complexity of the catalytic sites for Mo_1Fe_1Pd sample, the Gibbs free energy diagrams for NO_3RR on Mo_1Pd and Fe_1Pd bimetallenes were first calculated (Table S3). As shown in Figures S33–S35, the RDSs on Fe_1Pd and Mo_1Pd are $*NO + H^+ + e^- \rightarrow *NHO$ ($\Delta G_{max} = 0.89$ eV) and $*NH_2 + H^+ + e^- \rightarrow * + NH_3$ ($\Delta G_{max} = 1.03$ eV) in NO_3RR, respectively. The results indicate that $NO_2^- \rightarrow NH_3$ conversion is inhibited on Mo_1Pd, hence NO_2^- prefers to be obtained. In contrast, the energy barrier of the RDS on Fe_1Pd is lower than that on Mo_1Pd, $*NO_2$ has a larger tendency to be converted to NH_3. The above results well explain the larger $j_{NO_2^-}$ for Mo_1Pd and larger j_{NH_3} for Fe_1Pd (Figure 4a,b).

Based on the above analysis, the Gibbs free energy diagrams for NO_3RR on Mo_1Fe_1Pd were further calculated. Notably, Mo and Fe sites were co-existed, energy diagrams on Mo and Fe sites for Mo_1Fe_1Pd (Figures 5a, S36, S37, and Table S3) were calculated, respectively. The RDSs are $*NO \rightarrow *NHO$ and $*NHOH \rightarrow *NH_2OH$ with energy barrier of 0.62 and 0.33 eV on Mo and Fe sites, respectively. From the above results, it is reasonably inferred that N-intermediates may experience different catalytic sites from the viewpoint

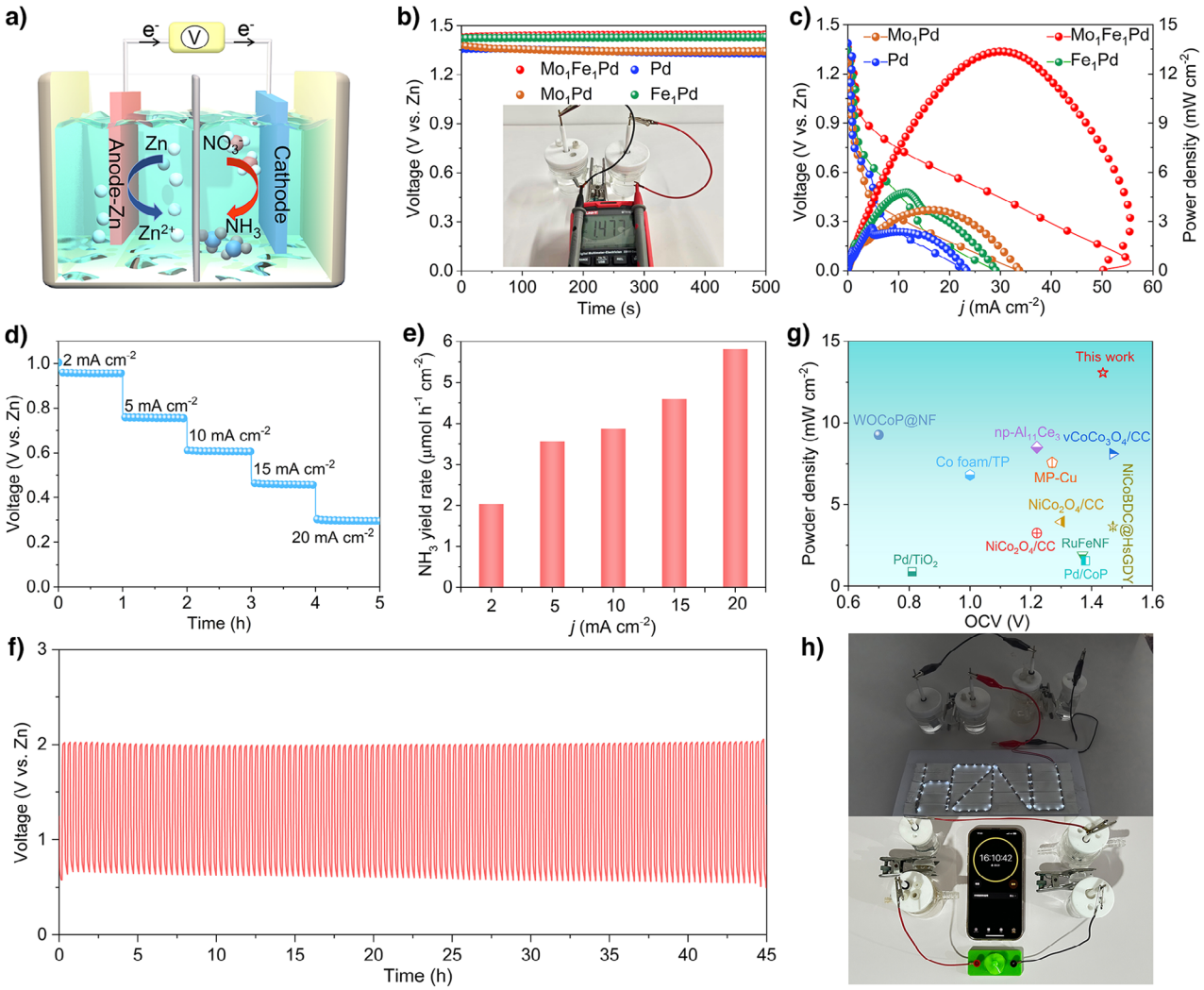

Figure 6. a) The schematic illustration for the assembled Zn-NO_3^- battery with Zn anode and Mo_1Fe_1Pd trimetallene cathode. b) Open-circuit voltage of Zn-NO_3^- battery, c) discharging polarization curves and the resultant power densities of the battery using the Mo_1Fe_1Pd, Mo_1Pd, Fe_1Pd and Pd metallenes cathodes, the inset in b shows the voltage determined by avometer. d) Rate performance of Zn-NO_3^- battery using Mo_1Fe_1Pd trimetallene as cathode. e) NH_3 yield rates derived from the Zn-NO_3^- battery system at different discharge current densities. f) Discharge-charge processes of the Zn-NO_3^- battery at a constant current density of 2 mA cm^{-2}. g) The comparison of the open-circuit voltage and the powder density for Mo_1Fe_1Pd trimetallene with the recently reported electrocatalysts. h) Photographs of LEDs and a mini fan motor powered by the Zn-NO_3^- battery.

of the minimum energy principle. To further support the conclusion, the adsorption energy of all the N-intermediates in NO_3RR were calculated and compared. As shown in Figure 5b, *NHO and *NH_2 intermediates prefer to adsorb on Fe site with larger adsorption energies, while the other N-intermediates tend to adsorb on Mo site in the case of coexistence of Mo and Fe sites, i.e., Mo_1Fe_1Pd sample. The result suggests that N-intermediates may hop back and forth between Mo and Fe sites in NO_3RR. Therefore, the optimal pathway of NO_3RR for Mo_1Fe_1Pd is achieved on alternant Mo and Fe sites, and the RDS is changed to *NO→*NHO with the ultralow ΔG_{max} value of 0.12 eV (Figure 5c).

As summarized in Figure 5d, NO_3^- is initially adsorbed on Mo site for Mo_1Fe_1Pd, and then hydrogenated step by step to *NO (Mo site). Subsequently, *NO is further hydrogenated to *NHO and adsorbed on Fe site, followed by spillover to Mo site, and *NHOH is adsorbed on Mo site. After hydrogenation of *NHOH to *NH_2OH on Mo site, NH_2OH is dehydrated and spilled over to Fe site again. Finally, NH_3 is formed through one step hydrogenation and desorption processes. The reaction intermediates spill over three times between Mo and Fe sites in the entire NO_3RR process, ultimately avoiding the large energy barriers of the RDS on Mo_1Pd and Fe_1Pd. Benefitting from the continuous intermediates spillover effect, the RDS on Mo_1Fe_1Pd is changed to *NO→*NHO with ultralow energy barrier of 0.12 eV, much lower than that of Mo_1Pd and Fe_1Pd samples. As such, electrochemical NO_3RR on Mo_1Fe_1Pd is greatly accelerated, aligned with the partial current density results (Figure 4a,b).

To investigate the electronic structure of dual single-atom alloy metallene, projected density of states (PDOS) of metal valence orbitals in Fe_1Pd, Mo_1Pd, and Mo_1Fe_1Pd were calculated and compared (Figure 5e). The results

demonstrated that Mo_1Pd exhibited higher d-band center (ε_d = −2.18 eV) than Fe_1Pd (ε_d = −2.41 eV), and the ε_d value of Mo_1Fe_1Pd was adjusted to a moderate level of −2.25 eV due to the co-doping of atomic Mo and Fe atoms, which can effectively regulate the interaction between metal active sites and the reaction intermediates. Based on the single active site, the adsorption energies of the N-intermediates exhibited obvious linear scaling relationship between Fe_1Pd and Mo_1Pd (Figure 5f). Moreover, Mo_1Pd owned stronger adsorption of intermediates compared to Fe_1Pd, which was the primary reason why NH_3 desorption was the RDS for Mo_1Pd. The adsorption energies of the different intermediates on Fe_1Pd, Mo_1Pd, and Mo_1Fe_1Pd were compared and displayed in Figure 5g. The results suggest that dual single-atom Mo and Fe sites in Mo_1Fe_1Pd can break the linear adsorption of intermediates on the single active site, which plays an important role in enhancing the electrocatalytic activity for NO_3RR. Therefore, the co-doping of Mo and Fe atoms in Pd metal can be considered an effective strategy for enhancing the electrocatalytic performance in NO_3RR through regulating of electronic structure. In addition, the water splitting process for *H supply was also calculated (Figure S38 and Table S4). $*H_2O \rightarrow *OH + *H$ process occurred on $Fe_1Pd(111)$ or Fe site-$Mo_1Fe_1Pd(111)$ all delivered lower energy barriers than that of $Mo_1Pd(111)$ and Mo site-$Mo_1Fe_1Pd(111)$, suggesting Fe doping in Pd matrix indeed facilitates H—OH bond breakage. As a result, the kinetics of NO_3RR to NH_3 conversion was accordingly improved, consistent with the variation trend of the partial current density (Figure 4c).

The excellent NO_3RR performance of Mo_1Fe_1Pd trimetallene enables the exploration of NO_3RR in a zinc-nitrate (Zn-NO_3^-) battery. A hybrid aqueous Zn-NO_3^- battery catalyzed by Mo_1Fe_1Pd trimetallene was assembled combined with a Zn anode (Figure 6a). The anolyte was 3 M KOH solution and the catholyte was 3 M KOH + 0.5 M KNO_3. The assembled Zn-NO_3^- battery delivered a stable open-circuit voltage (OCV) of 1.477 V, higher than that of Mo_1Pd, Fe_1Pd, and Pd metallenes electrodes (Figure 6b). A maximum discharge power density of 13.4 mW cm^{-2} was achieved, higher than that of Mo_1Pd bimetallenes (3.7 mW cm^{-2}), Fe_1Pd bimetallens (4.8 mW cm^{-2}) and Pd metallenes (2.6 mW cm^{-2}) (Figure 6c). The rate capability of the battery was assessed at the current densities of 2, 5, 10, 15, and 20 mA cm^{-2}, demonstrating the excellent discharge stability (Figure 6d). To confirm Zn-NO_3^- battery was a device not only outputting electrical energy, but only producing valuable NH_3, NH_3 yield rates were obtained at different discharge current densities (Figure 6e). Importantly, the power density and the OCV of the battery were all higher than recently reported state-of-the-art results using transition metal based catalysts (Figure 6g and Table S5).

Zinc-nitrate battery was rechargeable, in which the dissolution and deposition of Zn on the anode and NO_3RR and ammonia/water oxidation on the cathode occurred during the discharge and charge processes, respectively.[49] Figure 6f shows the long-term charge and discharge curves of Mo_1Fe_1Pd trimetallene electrode at a current density of 2 mA cm^{-2}. Impressively, zinc-nitrate battery could achieve steady charge and discharge test for 45 h. Two batteries in series could light LED lights and drive the small fan continuously for 16 h (Figure 6h), demonstrating the excellent application prospect. In brief, the well-designed battery could work consecutively as an energy-chemical output device for practical ammonia production and continuous power output.

Conclusions

In summary, a highly efficient and durable dual single-atom Mo_1Fe_1Pd alloy metallene was synthesized for electrochemical nitrate conversion to ammonia. Atomically dispersed molybdenum and iron atoms in Pd lattice provided two distinct catalytic sites, enabling the continuous intermediates spillover between Mo and Fe sites. So that NO_3RR experienced the lowest energy barrier for each elementary step, which was confirmed by in situ spectroscopic characterizations and theoretical calculations. Furthermore, the co-doping of Mo and Fe atoms altered the interfacial water structure to restrain the competing HER, as well as regulated the electronic structure, resulting in high NH_3 yield rate and NH_3 FE synchronously. Mo_1Fe_1Pd trimetallene delivered a remarkable NH_3 yield rate of 13.4 mol $g_{cat.}^{-1}$ h^{-1} and NH_3 FE of 94.6%, as well as excellent cycling stability. Moreover, the assembled zinc-nitrate battery delivered an OCV of 1.477 V, and the maximum output power density of 13.4 mW cm^{-2}. This work provides new insights into the design of efficient, selective and durable electrocatalysts for multi-steps and multi-intermediates involved electrosynthesis process from the angle of intermediates hopping effect.

Acknowledgements

This work was financially supported in part by the National Natural Science Foundation of China (22309039, 22422112, 22371296, U21A2077), the University Leading Talents Program of Zhejiang Province (4095C502222140203, 4095C502222140201), the Medical Health Science and Technology Project of the Zhejiang Provincial Health Commission (2023KY1009), the Natural Science Foundation of Shandong Province (ZR2022JQ08, ZR2024MB003, 2023HWYQ-028), the Taishan Scholar of Shandong Province (tsqn202211028, tsqn202306080, tsqn202306126).

Conflict of Interests

The authors declare no conflict of interest.

Data Availability Statement

Research data are not shared.

Keywords: Dual single-atom alloy • Dynamic interaction • NO_3RR • Spillover • Zinc-nitrate battery

[1] W. Guo, K. Zhang, Z. Liang, R. Zou, Q. Xu, *Chem. Soc. Rev.* **2019**, *48*, 5658–5716.
[2] S. Li, Y. Zhou, X. Fu, J. B. Pedersen, M. Saccoccio, S. Z. Andersen, K. Enemark-Rasmussen, P. J. Kempen, C. D. Damsgaard, A. Xu, R. Sažinas, J. Mygind, N. H. Deissler, J. Kibsgaard, P. C. K. Vesborg, J. K. Nørskov, I. Chorkendorff, *Nature* **2024**, *629*, 92–97.
[3] G. Qing, R. Ghazfar, S. T. Jackowski, F. Habibzadeh, M. M. Ashtiani, C. Chen, M. R. Smith, III, T. W. Hamann, *Chem. Rev.* **2020**, *120*, 5437–5516.
[4] B. Li, Y. Zhu, W. Guo, *Inorg. Chem. Front.* **2023**, *10*, 5812–5838.
[5] Y. Xiong, Y. Wang, J. Zhou, F. Liu, F. Hao, Z. Fan, *Adv. Mater.* **2024**, *36*, 2304021.
[6] S. Tang, M. Xie, S. Yu, X. Zhan, R. Wei, M. Wang, W. Guan, B. Zhang, Y. Wang, H. Zhou, G. Zheng, Y. Liu, J. H. Warner, G. Yu, *Nat. Commun.* **2024**, *15*, 6932.
[7] H. Li, S. Li, R. Guan, Z. Jin, D. Xiao, Y. Guo, P. Li, *ACS Catal.* **2024**, *14*, 12042–12050.
[8] R. Li, T. Gao, P. Wang, W. Qiu, K. Liu, Y. Liu, Z. Jin, P. Li, *Appl. Catal. B: Environ.* **2023**, *331*, 122677.
[9] C. Han, L. Sun, S. Han, B. Liu, *Angew. Chem. Int. Ed.* **2024**, e202416910.
[10] J. Li, W. Yu, H. Yuan, Y. Wang, Y. Chen, D. Jiang, T. Wu, K. Song, X. Jiang, H. Liu, R. Hu, M. Huang, W. Zhou, *Nat. Commun.* **2024**, *15*, 9499.
[11] W. Zhong, Q. Hong, X. Ai, C. Zhang, F. Li, X. Li, Y. Chen, *Adv. Mater.* **2024**, *36*, 2314351.
[12] G. Wu, W. Zhang, R. Yu, Y. Yang, J. Jiang, M. Sun, A. Du, W. He, L. Dai, X. Mao, Z. Chen, Q. Qin, *Angew. Chem. Int. Ed.* **2024**, *63*, e202410251.
[13] S. Ren, R. Gao, N. T. Nguyen, L. Wang, *Angew. Chem. Int. Ed.* **2024**, *63*, e202317414.
[14] J. Yu, R. Gao, X. Guo, N. T. Nguyen, L. Wu, L. Wang, *Angew. Chem. Int. Ed.* **2025**, *64*, e202415975.
[15] K. Su, S. Ren, R. Gao, G. Bai, L. Wu, L. Wang, *Angew. Chem. Int. Ed.* **2025**, *64*, e202422443.
[16] Y. Yao, K. Wei, S. Zhao, H. Zhou, B. Kui, G. Zhu, W. Wang, P. Gao, W. Ye, *ACS Sustainable Chem. Eng.* **2025**, *13*, 1245–1252.
[17] S. Yin, Y. Xiao, X. Gu, Q. Hao, H. Liu, Z. Hao, G. Meng, X. Pan, Q. Pei, *Acta Geophys.* **2019**, *67*, 1191–1203.
[18] R. Zhang, Y. Guo, S. Zhang, D. Chen, Y. Zhao, Z. Huang, L. Ma, P. Li, Q. Yang, G. Liang, C. Zhi, *Adv. Energy Mater.* **2022**, *12*, 2103872.
[19] X. Guo, W. Zhang, J. Shi, M. Duan, S. Liu, J. Zhang, Y. Liu, S. Xiong, Q. Kong, *Nano Res.* **2022**, *15*, 2092–2103.
[20] W. Yu, J. Yu, M. Huang, Y. Wang, Y. Wang, J. Li, H. Liu, W. Zhou, *Energy Environ. Sci.* **2023**, *16*, 2991–3001.
[21] S. Li, J. Liang, P. Wei, Q. Liu, L. Xie, Y. Luo, X. Sun, *eScience* **2022**, *2*, 382–388.
[22] W. Zhu, F. Yao, Q. Wu, Q. Jiang, J. Wang, Z. Wang, H. Liang, *Energy Environ. Sci.* **2023**, *16*, 2483–2493.
[23] J. Ye, A. Wang, Y. Yang, X. Qian, C. Wan, G. He, H. Chen, *Chem. Eng. J.* **2024**, *487*,150434.
[24] Y. Zhou, L. Zhang, Z. Zhu, M. Wang, N. Li, T. Qian, C. Yan, J. Lu, *Angew. Chem. Int. Ed.* **2024**, *63*, e202319029.
[25] K. Zhang, Z. Zhang, T. Yang, S. Wang, S. Liu, Z. Zhao, S. Hu, Z. Ma, J. Huang, Y. Yang, Y. Chen, B. Ge, *ACS Appl. Mater. Interfaces* **2024**, *16*, 43526–43534.
[26] E. Murphy, Y. Liu, I. Matanovic, S. Guo, P. Tieu, Y. Huang, A. L. Das, l. Zenyuk, X. Pan, E. Spoerke, P. Atanassov, *ACS Catal.* **2022**, *12*, 6651–6662.
[27] J. Wan, H. Zhang, J. Yang, J. Zheng, Z. Han, W. Yuan, B. Lan, X. Li, *Appl. Catal. B: Environ.* **2024**, *347*, 123816.
[28] M. Luo, Z. Zhao, Y. Zhang, Y. Sun, Y. Xing, F. Lv, Y. Yang, X. Zhang, S. Hwang, Y. Qin, J. Ma, F. Lin, D. Su, G. Lu, S. Guo, *Nature* **2019**, *574*, 81–85.
[29] J.-G. Choi, L. T. Thompson, *Appl. Surf. Sci.* **1996**, *93*, 143–149.
[30] C. L. Bianchi, M. G. Cattania, P. Villa, *Appl. Surf. Sci.* **1993**, *70-71*, 211–216.
[31] X. Li, X. Li, C. Liu, H. Huang, P. Gao, F. Ahmad, L. Luo, Y. Ye, Z. Gen, G. Wang, R. Si, C. Ma, J. Yang, J. Zeng, *Nano Lett.* **2020**, *20*, 1403–1409.
[32] S. V. Lambeets, S. Pecaut, J. Kim, P. Zhu, Y. Z. Finfrock, D. M. Meira, G. King, G. Gao, W. Xu, D. A. Cullen, H. Zhou, Y. Han, D. E. Perea, C. L. Muhich, H. Wang, *Nat. Nanotechnol.* **2022**, *17*, 759–767.
[33] R. Y. Hodgetts, A. S. Kiryutin, P. Nichols, H. Du, J. M. Bakker, D. R. Macfarlane, A. N. Simonov, *ACS Energy Lett.* **2020**, *5*, 736–741.
[34] H. Jiang, G. Chen, O. Savateev, J. Xue, L. Ding, Z. Liang, M. Antonietti, H. Wang, *Angew. Chem. Int. Ed.* **2023**, *62*, e202218717.
[35] E. Skúlason, V. Tripkovic, M. E. Björketun, S. Gudmundsdóttir, G. Karlberg, J. Rossmeisl, T. Bligaard, H. Jónsson, J. K. Nørskov, *J. Phys. Chem. C* **2010**, *114*, 18182–18197.
[36] J. Zhu, L. Hu, P. Zhao, L. Lee, K. Wong, *Chem. Rev.* **2020**, *120*, 851–918.
[37] S. Han, H. Li, T. Li, F. Chen, R. Yang, Y. Yu, B. Zhang, *Nat. Catal.* **2023**, *6*, 402–414.
[38] R. Zhang, H. Hong, X. Liu, S. Zhang, C. Li, H. Cui, Y. Wang, J. Liu, Y. Hou, P. Li, Z. Huang, Y. Guo, C. Zhi, *Angew. Chem. Int. Ed.* **2023**, *62*, e202309930.
[39] F. Wang, H. Zhao, G. Zhang, H. Zhang, X. Han, K. Chu, *Adv. Funct. Mater.* **2024**, *34*, 2308072.
[40] W. Ye, Y. Zhang, L. Chen, F. Wu, Y. Yao, W. Wang, G. Zhu, G. Jia, Z. Bai, S. Dou, P. Gao, N. Wang, G. Wang, *Angew. Chem. Int. Ed.* **2024**, *63*, e202410105.
[41] Q. Hu, K. Yang, O. Peng, M. Li, L. Ma, S. Huang, Y. Du, Z. Xu, Q. Wang, Z. Chen, M. Yang, K. P. Loh, *J. Am. Chem. Soc.* **2024**, *146*, 668–676.
[42] K. Chen, Z. Ma, X. Li, J. Kang, D. Ma, K. Chu, *Adv. Funct. Mater.* **2023**, *33*, 2209890.
[43] R. Hao, L. Tian, C. Wang, L. Wang, Y. Liu, G. Wang, W. Li, G. A. Ozin, *Chem. Catal.* **2022**, *2*, 622–638.
[44] J. Ni, J. Yan, F. Li, H. Qi, Q. Xu, C. Su, L. Sun, H. Sun, J. Ding, B. Liu, *Adv. Energy Mater.* **2024**, *14*, 2400065.
[45] R. Gao, Z. Gao, N. T. Nguyen, J. Chen, X. Liu, L. Wang, L. Wu, *Nat. Sustain.* **2025**, 1–10, https://doi.org/10.1038/s41893-025-01530-y.
[46] Y. Wang, S. Zheng, W. Yang, R. Zhou, Q. He, P. Radjenovic, J. Dong, S. Li, J. Zheng, Z. Yang, G. Attard, F. Pan, Z. Tian, J. Li, *Nature* **2021**, *600*, 81–85.
[47] K. Zhu, J. Ma, L. Chen, F. Wu, X. Xu, M. Xu, W. Ye, Y. Wang, P. Gao, Y. Xiong, *ACS Catal.* **2022**, *12*, 4840–4847.
[48] L. Shen, B. Lu, Y. Li, J. Liu, Z. Huang-fu, H. Peng, J. Ye, X. Qu, J. Zhang, G. Li, W. Cai, Y. Jiang, S. Sun, *Angew. Chem. Int. Ed.* **2020**, *59*, 22397–22402.
[49] W. Kang, B. Zhang, Z. Wang, Z. Zhang, M. Niu, X. An, Z. Mou, X. Fan, X. Hu, B. Xi, S. Xiong, *J. Energy Chem.* **2024**, *94*, 608–617.

Manuscript received: April 27, 2025
Revised manuscript received: May 31, 2025
Accepted manuscript online: June 05, 2025
Version of record online: June 16, 2025